Check for updates

Atomically modulated Cu single-atom catalysts for oxygen reduction reactions towards high-power density Zn– and Al–air batteries†

Nayantara K. Wagh, Sambhaji S. Shinde* and Jung-Ho Lee [ID] *

Herein, Cu single-atom-encapsulated hollow carbon–nitrogen spheres (CuSA@CNS) are fabricated through a solution process, confining optimal electronic structures reinforcing Cu–N_4 active sites. CuSA@CNS demonstrate a remarkable half-wave potential of 0.95 V, mass activity, and a durability of 5000 cycles. Accordingly, CuSA@CNS present record-high power densities of 371 and 289 mW cm^{-2} for Zn– and Al–air batteries. The rechargeable Zn–air battery demonstrates an unprecedented small charge–discharge voltage and stable cycling for harsh operations at 50 mA cm^{-2}, outperforming Pt/C.

Zn–air (ZABs) and Al–air batteries (AABs) are the possible solutions because of their high energy density (1086 and 8100 W h kg^{-1}), cost-effectiveness, and significant durability.[1–4] However, the multi-step sluggish oxygen reduction reaction (ORR) kinetics and the high cost of commercial Pt-based catalysts limit their practical feasibility.[5,6] Significant efforts have been focused on determining Pt-free catalysts such as metal-free, transition metal (Fe, Co, Ni, Mn, and Cu)-based systems (oxides, nitrides, sulfides, carbides, metal–organic-frameworks, metal–nitrogen–carbon M–N–C, and hydroxides), and composite catalysts.[1–12]

Single-atom catalysts (SACs) have garnered extensive attention due to their exceptional atom utilization efficiency, distinct geometric configurations, unsaturated coordination environments, and tunable electronic properties.[9] The density of active sites and intrinsic activity are crucially determined by optimizing the geometric and electronic characteristics to enhance the SACs ORR performance. However, the formidable challenges are the atomic stability of isolated metal centres, the concurrent formation of less-active sites and inactive metal species during pyrolysis, and the poor utilization of active centres enclosed by carbon structures.[13,14] Local active-metal environments and electronic

Department of Materials Science and Chemical Engineering, Hanyang University, Ansan, Republic of Korea. E-mail: jungho@hanyang.ac.kr, physics.sambhaji2006@gmail.com
† Electronic supplementary information (ESI) available. See DOI: https://doi.org/10.1039/d4cc05217j

interactions play a decisive role in SACs ORR performance. Electronic structure modulation involving metal sites with specific coordination numbers, coordinated atoms, centered atoms, and the first or second coordination frameworks with centered atoms regulates the d orbitals and charge density redistribution of the active atom sites.[15,16]

Among SACs, Fe–N_4 is determined to be the most suitable for the ORR; however, it limits the O_2 adsorption and activation due to the symmetric configuration of Fe–N_4 sites or the Fenton effect. Thus, a considerable number of asymmetric-coordination-based Fe-SACs such as Fe–N_4, Fe–N_4P_1, and Fe–N_3S_1 have been developed, so that the ORR and ZAB performances are beyond those of the electrocatalysts.[8,17] Typically, the ORR follows the triple-phase interface; thus, electrocatalyst geometry critically influences the mass and electron transport. Microporous and mesoporous structures promote the fast shuttling of electrons and mass transport, respectively, which resist water intrusion during the ORR.[18] The relationship between intrinsic activities and structures for the mass-transport-controlled processes is reported rarely. Furthermore, dynamic switching of SACs governs the coordinating structures even for the same metal atoms.[19] Most of the reported ZABs or AABs achieved a power density of ~200 or ~100 mW cm^{-2}.[1–12] However, to compete with Li-ion batteries and realize long-term practical feasibility, further development of ORR catalysts is highly desirable. We need to explore a correlation between micro-to-nanoscale atomic structures, intrinsic activities, and dynamic growth to satisfy all the crucial requirements and enhance the overall performance instantly.

Here, we report a facile strategy for the rational construction of CuSA@CNS SACs towards proficient and robust hollow carbon–nitrogen frameworks through high utilization of Cu–N_3 active-sites, exceptional mass/electron transfer, and defect characteristics using solution processes. Atomic coordination of CuSA@CNS regulates the chemical and electronic structures of Cu-metal sites by optimizing the adsorption of oxygen intermediates, which improves the ORR performance. CuSA@CNS exhibit superior ORR activities and durability while outperforming Pt/C and other reported catalysts. ZABs and AABs
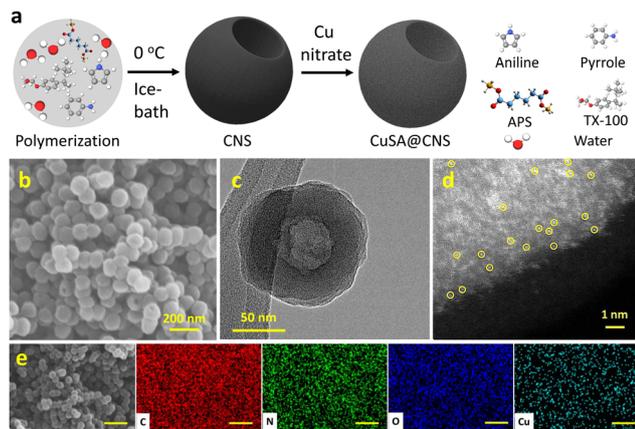
Fig. 1 Microscopy and structural characterization of CuSA@CNS. (a) Schematics of fabrication processes. (b) SEM, (c) STEM, and (d) Cs-corrected HAADF-STEM images of CuSA@CNS catalysts. (e) HAADF-STEM image and the elemental distribution maps for C, N, O, and Cu of CuSA@CNS. Scale: 400 nm.

Fig. 2 XPS spectra (a) C 1s, (b) N 1s, and (c) Cu 2p core-states of CuSA@CNS catalysts. (d) Fourier-transform EXAFS spectra of the Cu foil and CuSA@CNS in the R-space.

assembled with CuSA@CNS deliver the highest power densities of 371 and 289 mW cm^{-2} and energy densities of 1080 and 4290 W h kg^{-1}, respectively. Rechargeable ZABs with CuSA@CNS deliver a stability of 313 cycles under harsh operating conditions of 50 mA cm^{-2}.

Fig. 1a illustrates the schematics for the fabrication processes of CuSA@CNS catalysts. Triton^{TM} X-100 was dispersed uniformly in aqueous solution and then treated with aniline and pyrrole using an ice bath. Subsequently, an appropriate amount of ammonium persulfate was polymerized with initial suspensions to obtain hollow carbon–nitrogen nanospheres. After that, Cu single-atoms were incorporated into CNS frameworks by ultrasonication and successive pyrolysis under an inert atmosphere at 160 °C (see experimental methods for details, ESI†). Scanning and transmission electron microscopy (SEM and TEM) images display the three-dimensional hollow carbon–nitrogen spheres of 50–150 nm diameters with and without Cu single-atoms (Fig. 1b, c and Fig. S1, S2, ESI†). The aberration-corrected HAADF-STEM image exhibits bright spots (yellow circles) without Cu aggregation, indicating the formation of Cu single-atoms (Fig. 1d and Fig. S3, ESI†). SEM and energy-dispersive X-ray spectroscopy (EDS) maps display uniform distributions of C, N, O, and Cu elements (Fig. 1e). The X-ray diffraction (XRD) patterns illustrate amorphous graphitic carbon frameworks (Fig. S3, ESI†). Inductively coupled plasma optical emission spectrometry (ICP-OES) confirms a Cu loading of 5.5 wt%. Nitrogen adsorption–desorption and pore size distribution isotherms reveal the presence of micro- and mesopores with C–N frameworks. Brunauer–Emmett–Teller (BET) analysis reveals a surface area of 531 m^2 g^{-1} for CuSA@CNS (Fig. S4, ESI†).

The elemental composition and chemical states were determined by using X-ray photoelectron spectroscopy (XPS). Survey scan XPS spectra confirm the presence of C, N, O, and Cu elements with a composition of 62.30, 22.94, 9.16, and 5.60 at% for CuSA@CNS, respectively (Fig. S5a and Table S1, ESI†). The high-resolution C 1s spectra (Fig. 2a) of CuSA@CNS display the
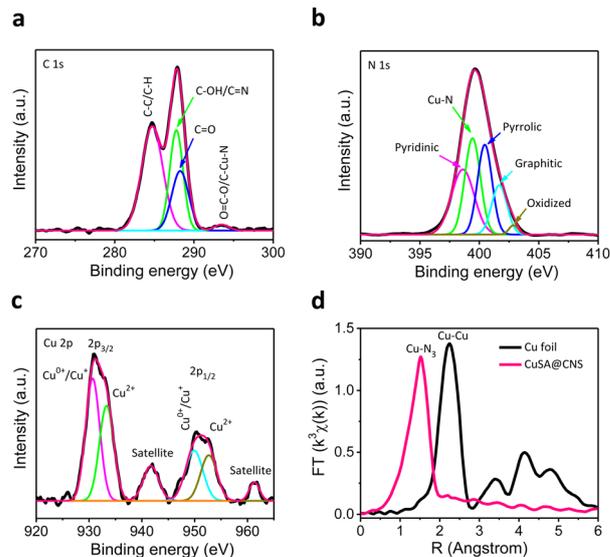
characteristic species of C–C/C–H (284.7 eV), C–OH/C═N (287.5eV), C═O (288.3 eV), O═C–O or C–Cu–N (293.4 eV).[20] The N 1s spectra exhibit the characteristic peaks of 398.6, 399.4, 400.4, 401.7, and 402.8 eV attributed to pyridinic N, Cu–N, pyrrolic N, graphitic N, and oxidized N, respectively (Fig. 2b). Among these, pyridinic N is responsible for the formation of isolated Cu–Nx sites. Graphitic N favours electron transfer, whereas abundant edge-type N facilitates the anchoring of Cu single-atoms for micro and mesoporous sites, which governs the significance of intrinsic ORR performances for Cu-sites.[8,21,22] Cu 2p spectra illustrate the Cu$^+$ and Cu^{2+} species with spin–orbit doublets of Cu 2p$_{3/2}$ (930.7 and 933.6 eV) and Cu 2p$_{1/2}$ (949.8 and 952.6 eV) with satellite peaks, implying the Cu–N and minor Cu–O intrinsic active sites (Fig. 2c).[5,23] O 1s spectra (Fig. S5b, ESI†) display peaks ascribed to ketonic [C–C(O)–C], hydroxyl O–H, ethers (C–O–C), ester–carbonyls (RCOO), ring oxygen, and oxygen along the carbonyl species with esters (–COO) at 529.7, 530.9, 532, 533.1, and 534.1 eV, respectively.[20,23] The electronic and chemical structures of Cu single-atoms in CuSA@CNS were obtained by X-ray absorption spectroscopy (XAS). Fourier transform (FT) extended X-ray absorption fine structure (EXAFS) spectra display a main peak of 1.52 Å that corresponds to the Cu–N first shell coordination with the Cu-coordinated number of ∼2.96 and positively charged Cu single-atoms in CuSA@CNS, illustrating the dominant Cu–N$_3$ configuration. The absence of Cu aggregation (or Cu–Cu binding) in CuSA@CNS related to the Cu foil verifies the atomic dispersion of Cu single-atoms.[6,24] Combined XPS and XAS analyses validated isolated Cu–N$_3$ active sites for oxygen electrocatalysis with asymmetric structures owing to the partial symmetry of micro- and mesoporous anchoring sites.

Electrocatalytic ORR performances of CuSA@CNS and controlled Pt/C were determined using rotating disk electrodes (RDEs) in an O$_2$-saturated KOH electrolyte (0.1 M). Fig. 3a
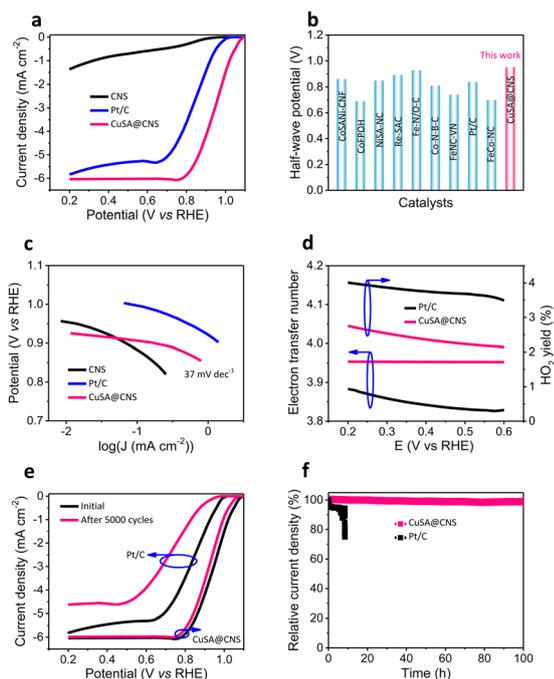
Fig. 3 ORR electrochemical performances. (a) LSV profiles of CuSA@CNS associated with those of CNS and reference Pt/C catalysts. (b) Ragone plots of ORR half-wave potentials. (c) Tafel slopes. (d) The electron transfer number and peroxide yield. (e) ORR accelerated durability. (f) The i–t stability measurements.

displays the linear scan voltammetry (LSV) polarization curves of CuSA@CNS, CNS, and Pt/C (20%). The CuSA@CNS catalyst demonstrates an outstanding half-wave potential of 0.95 V, surpassing Pt/C (0.84 V), CNS, reported single-atoms (*e.g.*, Fe, Cu, Ni, Co, re, Mn, and Zn) and other champion catalysts (Fig. 3b and Table S2, ESI†). This feature indicates the significant utilization of Cu–N$_3$ active sites and defect kinetics. CuSA@CNS exhibit a kinetic current density of 8.23 mA cm^{-2}, 4.3 times higher than that of Pt/C (1.89 mA cm^{-2}). CuSA@CNS exhibit a lower Tafel slope (37 mV dec^{-1}) and charge-transfer resistance (7 Ω) compared to those of Pt/C, illustrating a reduced O–O binding energy and superior ORR kinetics of Cu–N sites (Fig. 3c and Fig. S7, ESI†). The ORR selectivity and electron transfer numbers (n) of CuSA@CNS were determined using a rotating ring disk electrode (RRDE, Fig. 3d and Fig. S7, ESI†). Fig. 3c displays a 2.8% HO$_2^-$ yield for CuSA@CNS, validating exceptional selectivity for OH– compared to those of Pt/C and other catalysts with favourable catalytic processes. Four-electron transfer pathways for the ORR were detected for CuSA@CNS (3.96–4.0) and Pt/C (3.8–3.9) using the RRDE for a wide-potential range similar to the Koutecky–Levich equation. After 5000 accelerated durability testing (ADT) cycles, CuSA@CNS display excellent stability (<30 mV loss in $E_{1/2}$), compared to Pt/C (>160 mV, Fig. 3e). The long-term i–t test presents a retention of 98% final relative current for CuSA@CNS after 100 h, whereas Pt/C retains 73% in 9 h, manifesting superior ORR stability (Fig. 3f). No obvious changes in the morphological and valence states of the Cu–N sites in CuSA@CNS from TEM, EDS maps, and XPS after 5000

ADT cycles demonstrate the retention of Cu-atoms, validating superior durability (Fig. S8–S10, ESI†).

Theoretically, the d-band centers of Cu SAs (−2.46 eV) are comparable to those of Pt (−2.67 eV) catalysts and the partial removal of pyridinic N correlates with a higher electron density towards the neighboring single atoms.[24] Then, Cu SAs improve the nucleophile strength of C–N with oxygen intermediates compared to Co, Fe, or other metals, consistent with experimental results (Table S2, ESI†), illustrating superior ORR kinetics. To determine the practical performances of CuSA@CNS catalysts, the alkaline ZABs and AABs were assembled with CuSA@CNS cathodes. CuSA@CNS-based ZABs afforded the highest current density of 600 mA cm^{-2} with a record-breaking power density of 371 mW cm^{-2} and an open-circuit potential of 1.57 V, which were significantly improved compared to those of Pt/C (154 mW cm^{-2}) and reported champion catalysts (Fig. 4a and Table S3, ESI†). Fig. 4b displays stable high discharge potentials for CuSA@CNS at a current density of 10–100 mA cm^{-2}, and they recover the same discharge potential when reversed back to 10 mA cm^{-2}. CuSA@CNS-based ZABs deliver a specific capacity of 783 mA h g^{-1} that corresponds to an energy density of 1080 W h kg^{-1} for 20 mA cm^{-2} (Fig. 4c), surpassing that of the reference Pt/C (a capacity of 712 mA h g^{-1} and an energy density of 904 W h kg^{-1}). CuSA@CNS-based ZABs exhibit stable galvanostatic charge–discharge cycling with high voltage efficiency (59%) for 313 cycles (53 h) under harsh operating conditions of 50 mA cm^{-2}, whereas the Pt/C + RuO$_2$ performance drops severely within 5 h (Fig. 4d and Fig. S11, ESI†), validating the remarkable stability of CuSA@CNS ZABs. The Ragone plot displays exceptional power and energy densities with harsh operational feasibility compared to those of reported champion catalysts (Fig. 4e and Table S3, ESI†).[1–7,12–15,25,26] CuSA@CNS catalysts did not exhibit any structural or morphological changes after charge–discharge cycling (Fig. S12, ESI†).

For AABs, the CuSA@CNS exhibit an exceptional power density of 289 mW cm^{-2} for a current density of 400 mA cm^{-2} and an open-circuit voltage of 1.79 V, which also surpass those of Pt/C (177 mW cm^{-2} for 290 mA cm^{-2}). Moreover, AABs with CuSA@CNS display a high specific capacity of 2494 mA h g^{-1} and a corresponding energy density of 4290 W h kg^{-1} for 5 mA cm^{-2} outperforming Pt/C (a capacity of 1802 mAh g^{-1} and an energy density of 2108 W h kg^{-1}) and other reported catalysts (Table S4, ESI†). Fig. 4g illustrates the remarkable discharge rate performances and reversibility of CuSA@CNS, indicating the improved stability of alkaline AABs. This high-power density of ZABs and AABs is ascribed to major parameters such as: 1. atomic Cu–N coordination that improves the intrinsic ORR activity per site, 2. a large surface area that enables the utilization and exposure of catalytic active sites to a large extent, and 3. micro and mesoporous structures that protect Cu single-atoms from dissolution and enable accessibility to O–O.

In summary, we report the rational fabrication of CuSA@CNS catalysts with Cu single-atoms. The obtained CuSA@CNS demonstrate outstanding ORR performances and long-term durability. Alkaline ZABs and AABs with CuSA@CNS demonstrate record-high power densities of 371 and 289 mW cm^{-2}, specific capacities of 793 and 2494 mA h g^{-1}, and energy densities of 1080 and 4290 W h kg^{-1}, respectively. Moreover, the assembled ZABs show
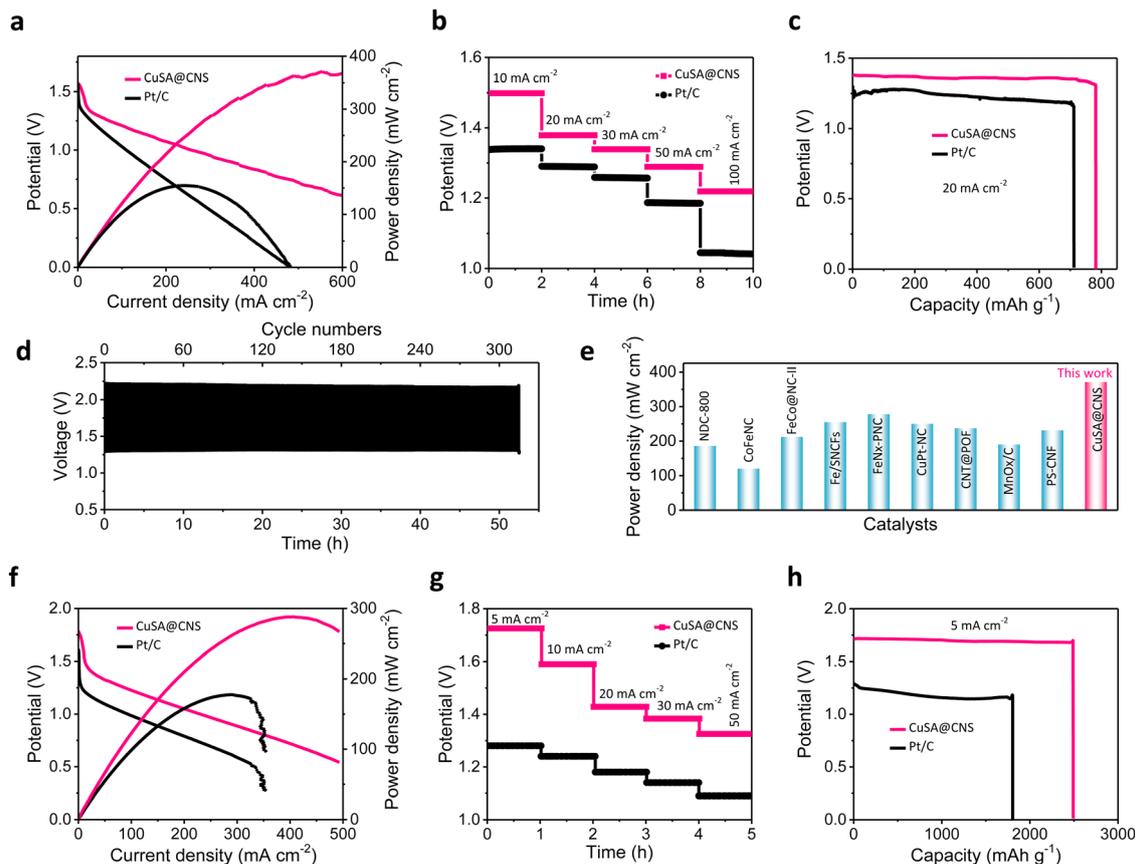
Fig. 4 (a) Discharge and power density characteristics of ZABs with CuSA@CNS and reference Pt/C. (b) Rate capacities of ZABs in the range of 10 to 100 mA cm^{-2}. (c) Specific capacity and energy density polarization of CuSA@CNS and Pt/C catalyst-based ZABs. (d) Cycle life performances of CuSA@CNS//KOH//Zn cells for a current rate of 50 mA cm^{-2}. (e) Ragone plots of power densities compared to previous champion reports. (f) Discharge and power density characteristics of AABs with CuSA@CNS and reference Pt/C cathodes. (g) Rate capacities. (h) Specific capacity and energy density polarization of CuSA@CNS and Pt/C catalyst-based AABs with the KOH electrolyte and Al anodes at 5 mA cm^{-2}.

313 cycles under harsh operating conditions of 50 mA cm^{-2}, highlighting their promising potential for practical applications.

Data availability

The data supporting this article have been included as part of the ESI.†

Conflicts of interest

There are no conflicts to declare.

Notes and references

1 S. Shinde, *et al.*, *Adv. Mater.*, 2023, **35**, 2303509.
2 S. Shinde, *et al.*, *Adv. Sci.*, 2023, **10**, 2304235.
3 Y. Xu, *et al.*, *Energy Storage Mater.*, 2024, 103772, DOI: **10.1016/j.ensm.2024.103772**.
4 S. Shinde, *et al.*, *Nat. Energy*, 2021, **6**, 592–604.
5 C. Liang, *et al.*, *Adv. Energy Mater.*, 2024, **14**, 2303935.
6 Y. Li, *et al.*, *Nat. Commun.*, 2024, **15**, 8365.
7 S. Shinde, *et al.*, *Energy Environ. Sci.*, 2019, **12**, 727–738.
8 P. Zhang, *et al.*, *Nat. Commun.*, 2024, **15**, 2062.
9 H. Tian, *et al.*, *Adv. Mater.*, 2023, **35**, 2210714.
10 Y. Li, *et al.*, *Adv. Mater.*, 2018, **30**, 1804653.
11 N. Wagh, *et al.*, *Nanoscale Horiz.*, 2023, **8**, 921–934.
12 N. Wagh, *et al.*, *Nano-Micro Lett.*, 2022, **14**, 190.
13 L. Jiao, *et al.*, *Nat. Mater.*, 2021, **20**, 1385.
14 Q. Yang, *et al.*, *J. Am. Chem. Soc.*, 2022, **144**, 2171.
15 C. Tang, *et al.*, *J. Am. Chem. Soc.*, 2021, **143**, 7819.
16 F. Wu, *et al.*, *J. Am. Chem. Soc.*, 2020, **142**, 16861.
17 J. Sheng, *et al.*, *ACS Nano*, 2022, **16**, 15994–16002.
18 Q. Zhang, *et al.*, *Science*, 2022, **378**, 181–186.
19 M. Liu, *et al.*, *Nat. Commun.*, 2024, **15**, 1675.
20 B. Sivaranjini, *et al.*, *Sci. Rep.*, 2018, **8**, 8891.
21 N. Wagh, *et al.*, *ACS Nano*, 2021, **15**, 14683.
22 S. Chen, *et al.*, *J. Am. Chem. Soc.*, 2022, **144**, 14505–14516.
23 D. Briggs and G. Beamson, *Anal. Chem.*, 1993, **65**, 1517.
24 N. Wagh, *et al.*, *Appl. Catal., B*, 2020, **268**, 118746.
25 S. Shinde, *et al.*, *ACS Nano*, 2018, **12**, 596–608.
26 S. Shinde, *et al.*, *ACS Nano*, 2017, **11**, 347–357.